

**Urbanization-induced urban heat island and aerosol effects on  
climate extremes in the Yangtze River Delta Region of China**

Shi Zhong<sup>1,2</sup>, Yun Qian<sup>2\*</sup>, Chun Zhao<sup>2,6</sup>, Ruby Leung<sup>2</sup>, Hailong Wang<sup>2</sup>, Ben Yang<sup>3,2</sup>, Jiwen  
Fan<sup>2</sup>, Huiping Yan<sup>4,2</sup>, Xiu-Qun Yang<sup>3</sup>, and Dongqing Liu<sup>5</sup>

<sup>1</sup> State Key Laboratory of Hydrology-Water Resources and Hydraulic Engineering, Center for  
Global Change and Water Cycle, Hohai University, Nanjing, China

<sup>2</sup> Pacific Northwest National Laboratory, Richland, WA, USA

<sup>3</sup> School of Atmospheric Sciences, Nanjing University, Nanjing, China

<sup>4</sup> College of Atmospheric Science, Nanjing University of Information & Technology, Nanjing,  
China

<sup>5</sup> Nanjing Meteorological Bureau, Nanjing, China

<sup>6</sup> University of Science and Technology of China, Hefei, China

Corresponding author: Yun Qian [Yun.Qian@pnnl.gov]

Submitted to *Atmospheric Chemistry and Physics*

October 1, 2016

20 **Abstract**

21       The WRF-Chem model coupled with a single-layer Urban Canopy Model (UCM) is  
22 integrated for 5 years at convection-permitting scale to investigate the individual and combined  
23 impacts of urbanization-induced changes in land cover and pollutants emission on regional  
24 climate in the Yangtze River Delta (YRD) region in eastern China. Simulations with the  
25 urbanization effects reasonably reproduced the observed features of temperature and  
26 precipitation in the YRD region. Urbanization over the YRD induces an Urban Heat Island (UHI)  
27 effect, which increases the surface temperature by 0.53 °C in summer and increases the annual  
28 heat wave days at a rate of 3.7 d/yr in the major megacities in the YRD, accompanied by  
29 intensified heat stress. In winter, the near-surface air temperature increases by approximately 0.7  
30 °C over commercial areas in the cities but decreases in the surrounding areas. Radiative effects  
31 of aerosols tend to cool the surface air by reducing net shortwave radiation at the surface.  
32 Compared to the more localized UHI effect, aerosol effects on solar radiation and temperature  
33 influence a much larger area, especially downwind of the city-cluster in the YRD.

34       Results also show that the UHI increases the frequency of extreme summer precipitation  
35 by strengthening the convergence and updrafts over urbanized areas in the afternoon, which  
36 favor the development of deep convection. In contrast, the radiative forcing of aerosols results in  
37 a surface cooling and upper atmospheric heating, which enhances atmospheric stability and  
38 suppresses convection. The combined effects of the UHI and aerosols on precipitation depend on  
39 synoptic conditions. Two rainfall events under two typical but different synoptic weather patterns  
40 are further analyzed. It is shown that the impact of urban land-cover and aerosols on precipitation  
41 is not only determined by their influence on local convergence, but also modulated by large-scale  
42 weather systems. For the case with a strong synoptic forcing associated with stronger winds and

43 larger spatial convergence, the UHI and aerosol effects are relatively weak. When the synoptic  
44 forcing is weak, however, the UHI and aerosol effects on local convergence dominate. This  
45 suggests that synoptic forcing plays a significant role in modulating the urbanization-induced  
46 land-cover and aerosol effects on individual rainfall event. Hence precipitation changes due to  
47 urbanization effects may offset each other under different synoptic conditions, resulting in little  
48 changes in mean precipitation at longer time scales.

49

50

51

52

53

54

55

## 1. Introduction

Urbanization affects climate and hydrological cycle by changing land cover and surface albedo, which releases additional heat to the atmosphere, and by emitting air pollutants, which interact with clouds and radiation (e.g., Shepherd, 2005; Sen Roy and Yuan, 2009; Yang et al., 2011). The most discernible impact of urban land-use change is the urban heat island (UHI) effect that can result in a warmer environment over urban areas than the surrounding areas (Landsberg, 1981; Oke, 1987). In addition to the thermal perturbations, the UHI has been well documented to modify wind patterns (Hjemfelt, 1982), evaporation (Wienert and Kuttler, 2005), atmospheric circulations (Shepherd and Burian, 2003; Baik et al., 2007; Lei et al., 2008), and precipitation around urban areas (Braham, 1979; Inoue and Kimura, 2004). Previous studies have found an increase of warm-season precipitation over and downwind of major cities due to the expanded urban land cover (Huff and Changnon, 1972; Changnon, 1979; Zhong et al., 2015). Recent studies suggested that the underlying urban surface also affects the initiation and propagation of storms (Bornstein and Lin, 2000; Guo et al., 2006) and convective activities in city fringes (Baik et al., 2007; Shepherd et al., 2010).

Concurrently increases in population and anthropogenic activities over urbanized areas increase pollutant emissions and aerosol loading in the atmosphere. Atmospheric aerosols have long been recognized to affect surface and top of the atmosphere (TOA) radiative fluxes and radiative heating profiles in the atmosphere via aerosol-radiation interactions (ARI) (e.g., Coakley et al., 1987; Charlson et al., 1992; Hansen et al., 1997; Yu et al., 2006; Qian et al., 2006, 2007, 2015; McFarquhar and Wang, 2006), which tend to induce cooling near the surface and heating at the low and mid-troposphere (Qian et al., 2006; Bauer and Mennon, 2012). Anthropogenic aerosols can also affect clouds and precipitation via aerosol-cloud interactions

79 (ACI) (e.g., Rosenfeld, 2000, 2008; Qian et al., 2010; Fan et al., 2013; 2015; Tao et al., 2012;  
80 Zhong et al., 2015). Localized changes in precipitation by strong aerosol perturbations can  
81 induce cold pools by evaporation, which may alter the organization of stratocumulus clouds (e.g.,  
82 Wang and Feingold, 2009; Feingold et al., 2010). Aerosol impacts on deep convective clouds are  
83 complicated by the interactions among dynamical, thermodynamical, and microphysical  
84 processes. For example, deep convection could be invigorated by aerosols as more cloud water  
85 associated with the smaller cloud drops is carried to higher levels where it freezes and releases  
86 more latent heat in a polluted environment (Rosenfeld, 2008; Khain, 2009; Storer and van den  
87 Heever, 2013). Fan et al. (2013) revealed a microphysical effect of aerosols from reduced fall  
88 velocity of ice particles that explains the commonly observed increases in cloud top height and  
89 cloud cover in polluted environments. Therefore, urbanization may influence precipitation and  
90 circulation through multiple pathways that are more difficult to disentangle than the dominant  
91 effect on temperature.

92 As one of the most developed regions in China, the Yangtze River Delta (YRD) has been  
93 experiencing rapid economic growth and intensive urbanization process during the past three  
94 decades. With the highest city density and urbanization level in China, the YRD has become the  
95 largest adjacent metropolitan areas in the world. It covers an area of  $9.96 \times 10^4 \text{ km}^2$ , with a total  
96 urban area of  $4.19 \times 10^3 \text{ km}^2$  (Hu et al., 2009). Observations have shown that the urban land-use  
97 expansion in this region has induced a remarkable warming due to the significant UHI effect (Du  
98 et al., 2006; Wu and Yang 2012, Wang et al., 2015). The annual mean warming reached up to  
99  $0.16^\circ\text{C}/10\text{yr}$  based on station measurements in large cities (Ren et al., 2008), which accounted  
100 for 47.1% of the overall warming during the period of 1961-2000. Urbanization in the YRD was  
101 found to destabilize the atmospheric boundary layer (Zhang et al., 2010) and enhance convection

and precipitation (Yang et al., 2012, Wan et al., 2013). Meanwhile, human activities associated with the ever-growing population have led to a dramatic increase in air pollutant emissions (Wang et al., 2006). Several observational and numerical studies have revealed that additional aerosol loading in this region could reduce solar radiation reaching the surface (Che et al., 2005; Qian et al., 2006, 2007), modify warm cloud properties (Jiang et al., 2013), and suppress light rainfall events (Qian et al., 2009).

The individual effects of urbanization-induced UHI and aerosol emission on local and regional climate have been examined separately in several modeling studies using short simulations of selected weather episodes at high spatial resolution or multiple-year climate simulations at coarse resolution. To more robustly quantify the urbanization-induced UHI and aerosol effects, convection-permitting simulations may reduce uncertainties in representing convection and its interactions with aerosols, which are parameterized in coarse-resolution models. Additionally, multi-year simulations are needed to understand and quantify the overall effects of land-cover change and aerosols in different large-scale environments (Oleson et al., 2008). In this study, a state-of-the-art regional model coupled with online chemistry (WRF-Chem) and a single-layer Urban Canopy Model (UCM) is used to simulate climate features in the YRD region. The climatic effects of the separate and combined land-cover and aerosol changes induced by urbanization are investigated using a set of 5-year (2006-2010) simulations with a horizontal resolution at convection-permitting scale (3 km). The paper is organized as follows. Section 2 describes the model configuration, experiment design, and model evaluation. The urbanization effects on extreme temperature and precipitation are presented in Section 3, followed by a summary of the conclusions in Section 4.

## 125 **2. Method**

### 126 **2.1 Model configuration**

127 The WRF-Chem model (Grell et al., 2005; Fast et al., 2006; Qian et al., 2010) simulates  
128 trace gases, aerosols and meteorological fields interactively (Skamarock et al., 2008; Wang et al.,  
129 2009), including aerosol-radiation interactions (Zhao et al., 2011, 2013a) and aerosol-cloud  
130 interactions (Gustafson et al., 2004). The coupled single-layer UCM (Kusaka et al., 2001; Chen  
131 et al., 2001) is a column model that uses a simplified geometry with two-dimensional,  
132 symmetrical street canyons to represent the momentum and energy exchanges between the urban  
133 surface and the atmosphere. The RADM2 (Regional Acid Deposition Model 2) gas chemical  
134 mechanism (Stockwell et al., 1990) and the MADE (Modal Aerosol Dynamics Model for  
135 Europe) and SORGAM (Secondary Organic Aerosol Model) aerosol module (Schell et al., 2001)  
136 are used. Detailed configuration of the above models can be found in Zhao et al. (2010). No  
137 cumulus parameterization is used at the convection-permitting resolution. The physical  
138 parameterization schemes used in our simulations are listed in Table 1.

### 139 **2.2 Numerical experiments**

140 Simulations are performed over a model domain centered at (120.50 °E, 31.00 °N) with a  
141 horizontal grid spacing of 3 km and 50 vertical levels extending from the surface to 50 hPa. The  
142 lowest 10 model layers are placed below 1 km to ensure a fine vertical resolution within the  
143 planetary boundary layer. Initial and boundary conditions for meteorological fields are derived  
144 from the National Center for Environmental Prediction (NCEP) FNL global reanalysis data on  $1^\circ$   
145  $\times 1^\circ$  grids at 6-hour interval. Lateral boundary conditions for chemistry are provided by a quasi-

146 global WRF-Chem simulation (Zhao et al., 2013b) that includes aerosols transported from  
147 regions outside the model domain.

148 The dominant land cover within each model grid cell is derived from the U.S. Geological  
149 Survey (USGS) 30 second dataset that includes 24-category land-use type, except that the land  
150 use over urban areas is updated using the stable nighttime light product (version 4) at 1 km  
151 spatial resolution (available at the National Geophysical Data Center,  
152 <http://ngdc.noaa.gov/eog/dmsp/downloadV4composites.html>). Corresponding to the value of  
153 lighting index of 25-50, 50-58, and >58 in the above product, each urban grid is identified as  
154 “Low Intensity Residential (LIR)”, “High Intensity Residential (HIR)”, or  
155 “Commercial/Industrial/Transportation (CIT)”, respectively. Figures 1a and 1b illustrate the  
156 urban area within the model domain for year 1970 and 2006, respectively. The anthropogenic  
157 heating (AH), characterized by a diurnal cycle with two peaks at rush hours of 0800 and 1700  
158 LST, respectively, is incorporated in the model simulations. The default maximum values of AH  
159 in WRF for LIR ( $20 \text{ W m}^{-2}$ ), HIR ( $50 \text{ W m}^{-2}$ ) and CIT ( $90 \text{ W m}^{-2}$ ) are used in this study (Tewari  
160 et al., 2007). Anthropogenic emissions of aerosols and their precursors are obtained from the  
161 Asian emission inventory (Zhang et al., 2009b), which is a  $0.5^\circ \times 0.5^\circ$  gridded dataset for 2006.  
162 Black carbon (BC), organic matter (OM), and sulfate emissions over China are extracted from  
163 the China emission inventory for 2008 (Lu et al., 2011), which provides monthly mean data on  
164  $0.1^\circ \times 0.1^\circ$  grids. It should be noted that the Noah land surface model defines a dominant land  
165 cover type for each grid, so no subgrid variability is simulated.

166 The anthropogenic emission fluxes of  $\text{SO}_2$  and BC in the simulation domain are shown in  
167 Figures 1c and 1d, respectively. Areas with large emissions are mainly located in four city  
168 clusters, i.e., Nanjing-Zhenjiang-Yangzhou, Suzhou-Wuxi-Changzhou, Shanghai, and Hangzhou



169 Bay, all inside the mega-city belt. Biomass burning emissions for the simulation period are  
170 obtained from the monthly Global Fire Emissions Database Version 3 (GFEDv3), which  
171 provides monthly mean data on  $0.5^\circ \times 0.5^\circ$  grids and the vertical distribution is determined by  
172 the injection heights described by Dentener et al. (2006) for the Aerosol Inter-Comparison  
173 project (AeroCom). Sea salt and dust emissions are configured following the same approach of  
174 Zhao et al. (2013b).

175 In order to investigate the individual responses of local and regional climate to land-cover  
176 change and increased aerosol loading, three experiments (i.e., LU06E06, LU70E70, and  
177 LU70E06) are conducted for 5 years from 2006 to 2010. The configurations of land use and  
178 aerosol emissions for these experiments are summarized in Table 2. All three simulations are  
179 performed using the same initial and boundary conditions and physics schemes, but with  
180 different land use types and/or anthropogenic emissions. LU06E06 is the control experiment,  
181 which represents the “present” (2006) urbanization level for both land use and aerosol/precursor  
182 emissions. LU70E06 uses the present aerosol emission data but with the land use of the 1970s,  
183 which is derived from the USGS dataset without the nighttime light correction. In LU70E70,  
184 both land use and emissions are set to the conditions of the 1970s. The differences of LU06E06-  
185 LU70E06, LU70E06-LU70E70, and LU06E06-LU70E70 can be used to derive the urban land-  
186 use effect, aerosol effect, and their combined effect, respectively (Table 3). The simulations are  
187 initialized on December 15 of each year during 2005-2009 to allow for a 16-day spin-up time  
188 and then continuously integrated for the next year (from January 1 to December 31). Results  
189 from January 1 to December 31 of all five years (2006-2010) are analyzed.

## 190 **2.3 Model evaluation**

191 The surface skin temperature simulated in LU06E06 is averaged over 2006-2010 and  
192 compared with the MODIS data. A spatial filtering method described by Wu and Yang (2012) is  
193 applied to isolate the heterogeneous climatic forcing of urbanization. More specifically, for each  
194 grid a spatial anomaly is defined as the departure from the average value over a region centered  
195 at each grid. Then, the moving spatial anomalies are calculated for all the grids with the moving  
196 region acting as a filtering window, which has a size of  $1^{\circ} \times 1^{\circ}$ . Figure 2 shows the moving  
197 spatial anomalies of mean surface skin temperature from MODIS observations and the L06E06  
198 simulation. The simulation captures the spatial distribution of observed surface skin temperature  
199 very well. In particular, the warmer centers over highly urbanized areas are well reproduced,  
200 despite slight underestimations in some mega cities in Zhejiang Province such as Hangzhou and  
201 Ningbo. Shanghai and Su-Xi-Chang exhibit the highest temperatures that are 2 °C above the  
202 surrounding rural areas.

203 To further validate the model, the baseline simulation LU06E06 is evaluated against  
204 meteorological station observations for 2006-2010. Figure 3 shows the averaged near-surface  
205 temperature and precipitation from observations and LU06E06. The simulated spatial pattern of  
206 near-surface air temperature agrees well with observations, with high temperature centers located  
207 at meteorological stations in major cities such as Shanghai and Hangzhou. The simulated  
208 temperature displays substantial spatial variability associated with heterogeneity in topography,  
209 land cover, and other regional forcings. The model captures the general north-to-south gradient  
210 of increasing precipitation in the observations. However, the model overestimates precipitation in  
211 Shanghai and central Jiangsu Province but underestimates the precipitation in the southwestern  
212 part of the domain.

213

## 214 **3. Results**

### 215 **3.1 Urbanization impact on surface temperature, radiation flux and heat waves**

#### 216 **3.1.1 Mean near-surface air temperature**

217         Figure 4 shows the differences in 2-meter near surface air temperature (T2m) among the  
218 three experiments to quantify the UHI and aerosol effects from urbanization (Table 3). The UHI  
219 effect causes an increase in near-surface temperature over the urbanized area in summer. The  
220 average temperature increase is about 0.53 °C over urban area and 1.49 °C in commercial areas  
221 outlined by the green contours (see Fig. 4a). In winter, the UHI warming effect occurs primarily  
222 in commercial areas, where the mean temperature increases by about 0.7 °C. In areas  
223 surrounding the central commercial region, however, temperature decreases due to the urban  
224 land-cover change (shown in Fig. 4d). Such a cooling effect in winter has also been found in  
225 previous studies (e. g., Oke, 1982; Jauregui et al., 1992; Wang et al., 2007). The “cool island”  
226 effects of urbanization during daytime in winter can be explained by the much larger surface  
227 thermal inertia of urban areas than that of rural areas with very low vegetation cover during  
228 winter (Wang et al., 2007). Although the wintertime cooling effect in urbanized area is not  
229 widely recognized, it is an important phenomenon that is also simulated by the model.

230         The increased aerosols induced by urbanization exert a cooling effect over the entire  
231 simulation domain in both summer and winter (Fig. 4b and 4e). On a domain average, the  
232 temperature reduction induced by increased aerosols is less than the warming induced by the  
233 UHI effect in both seasons. Therefore, the net urbanization impact (including both land-cover  
234 change and aerosol increase) on near-surface temperature is dominated by the UHI warming  
235 effect (Fig. 4c and 4f) resulted from the land-cover change in the YRD.

### 236 3.1.2 Surface solar radiation

237 The effects of urban land-cover change and increased aerosols on surface net shortwave  
238 radiation are shown in Fig. 5. As the building clusters reduce surface albedo (Oke, 1987), land-  
239 cover change increases the net shortwave radiation over urbanized areas, with an average  
240 increase of  $9.11 \text{ W m}^{-2}$  in summer and  $8.49 \text{ W m}^{-2}$  in winter. The net increase is greater in  
241 summer than in winter because of the stronger summertime incoming solar radiation. On the  
242 contrary, aerosols reduce the surface net shortwave radiation in the northern part of the domain  
243 corresponding to the larger  $\text{SO}_2$  and BC emission rates (Fig. 1), with a magnitude of  $8.79 \text{ W m}^{-2}$   
244 in summer and  $7.63 \text{ W m}^{-2}$  in winter. Different from the UHI effect that is more localized, the  
245 radiative impact of aerosols is more widespread and significant west of the major urban areas  
246 and even over the ocean. Figure 6 shows the spatial pattern of mean surface winds simulated in  
247 LU7006E7006 and the difference in column-integrated PM2.5 mass concentration between  
248 LU70E06 and LU70E70. Consistent with the prevailing monsoon circulation, southeasterly  
249 (northeasterly) flows dominate the YRD in summer (winter), which lead to increases in the  
250 PM2.5 concentration over the downwind area of the YRD city clusters. The increased PM2.5  
251 concentrations downwind of the YRD reduce solar radiation to the west (southwest) of the YRD  
252 in summer (winter), as shown in Figs. 5b and 5d. Hence aerosol effects on radiation are not  
253 limited to the emission source areas in metropolitan regions.

### 254 3.1.3 Heat waves

255 The UHI effect can significantly increase the near-surface temperatures in summer,  
256 thereby exacerbating extreme heat waves in urbanized areas (Stone, 2012). By definition, a heat  
257 wave occurs when the near-surface temperature reaches or exceeds  $35^\circ\text{C}$  for three or more

consecutive days (Tan et al., 2004). The averaged heat wave days comparing LU06E06 and LU70E06 increase at a rate of 3.7 d/yr in the major mega cities (Fig. 7a). The increase is most pronounced in Shanghai, with a rate larger than 12 d/yr.

High temperature during heat wave contributes to heat exhaustion or heat stroke, but the impact of atmospheric humidity on evaporation is also crucial. Here we use a heat stress index to assess the combined effects of temperature and humidity on human health due to the UHI effect, expressed as (Masterson and Richardson, 1979):

$$Humidex = Ta + (5/9)(e - 10) \quad (1)$$

where  $Ta$  is near-surface air temperature ( $^{\circ}\text{C}$ ) and  $e$  is water vapor pressure (hPa). Figure 7b depicts a big increase in heat stress index (Humidex) over urbanized regions in the YRD, except for the city of Hangzhou. The increase in heat stress index is more accentuated in Shanghai, with a mean increase of 2.16, relative to other urban areas. This suggests that humidity has a larger influence on heat stress in Shanghai because of its proximity to the ocean compared to urban areas further inland. In contrast, increased aerosols have little impact on heat waves (results not shown) because their impacts on near-surface temperature are much weaker (Fig. 4b).

### 3.2 Urbanization effects on summertime precipitation

#### 3.2.1 Long-term impact on extreme rainfall

Previous studies have provided evidence of urbanization effect on precipitation distribution in and around urban areas (e.g. Shepherd et al., 2003; Kaufmann et al., 2007; Miao et al., 2010). Several mechanisms have been proposed for the effects of urbanization on precipitation: (1) the UHI effect can destabilize the planetary boundary layer (PBL) and trigger

279 convection; (2) increased surface roughness may enhance atmospheric convergence that favors  
280 updrafts; (3) building obstruction tends to bifurcate rainfall systems and delays its propagation;  
281 (4) the change in land-cover decreases local evaporation, (5) anthropogenic emissions increase  
282 aerosol loading in the atmosphere, with subsequent effects on precipitation through changes in  
283 radiation and cloud processes. These mechanisms contribute to positive and negative changes in  
284 precipitation, leading to more complicated effects on precipitation than temperature.

285         In this section we analyze the results of the three 5-year simulations to examine the long-  
286 term impact of urbanization on precipitation. The results show that influences of both urban land  
287 cover and elevated aerosols on annual and seasonal mean precipitation are relatively small (not  
288 shown). This may be due to the urbanization effect for different rainfall events offsetting each  
289 other, leading to an overall weak effect on a longer time scale (see Section 3.2.2). Here we focus  
290 on the frequency of extreme rainfall over the YRD region. Extreme summer rainfall events are  
291 defined using hourly precipitation rate that is above 95<sup>th</sup> percentile at each grid for the period of  
292 2006-2010. Figure 8 shows the diurnal cycles of extreme rainfall frequency and urbanization-  
293 induced changes in the areas around Nanjing, Shanghai, and Su-Xi-Chang (shown in Fig. 1b).  
294 The frequency of hourly extreme rainfall reaches its maximum at around 16:00-17:00 LST over  
295 three urban clusters. Urban land-cover change increases the occurrence of extreme precipitation  
296 in the afternoon (12:00 to 20:00 LST). The maximum increase in the frequency of extreme  
297 hourly rainfall events for Nanjing, Shanghai, and Su-Xi-Chang can reach 0.86%, 1.09%, and  
298 0.79%, respectively, with the peak increase occurring in the late afternoon. On the contrary,  
299 aerosols exert an opposite impact to substantially reduce the frequency of extreme rainfall in the  
300 afternoon by up to 1.05%, 0.75%, and 0.72% for Nanjing, Shanghai, and Su-Xi-Chang,  
301 respectively. These impacts are significant compared to the maximum frequency of hourly

302 extreme rainfall of about 10% in each area. However, opposite effects of land-cover and aerosol  
303 emission changes result in a small net urbanization effect on extreme precipitation.

304 Because urbanization influences extreme precipitation primarily in the afternoon, we further  
305 analyze extreme rainfall events with a focus on the averages from 1200 to 2000 LST. Figure 9  
306 shows the substantial increase in extreme precipitation frequency concentrated over the major  
307 metropolitan areas in the YRD, with some compensation in the surrounding areas in general.  
308 Aerosols, however, reduce the occurrence of extreme precipitation more uniformly in most areas  
309 of the domain. The most significant influence of aerosols is found in the northwest part of the  
310 domain where aerosol concentrations increase the most downwind of the urban centers (Fig. 6a).  
311 Similar to the effects on surface temperature and solar radiation (Figs. 4 and 5), aerosols have a  
312 substantial impact on the occurrence of extreme precipitation over a wider area than the effects  
313 of urban land-use change.

314 How do changes in land cover and aerosols modulate extreme rainfall frequency? Figure  
315 10a shows the diurnal time-height cross section of the impact of urban land-cover (i.e., the  
316 difference between LU06E06 and LU70E06) on temperature and divergence averaged over the  
317 three city clusters (Nanjing, Shanghai, and Su-Xi-Chang). Air temperature over the urbanized  
318 areas increases significantly in the afternoon (from 1200 to 1800 LST) due to the UHI effect. The  
319 warming and the increased roughness length in urban areas favor convergence in the lower  
320 atmosphere and divergence above. As a result, the mean updraft increases over the urbanized  
321 areas in the afternoon (Fig. 10b), which increases cloud water from the lower to middle  
322 troposphere in the afternoon. Shortly before noon, there is a small reduction in low clouds, which  
323 may be related to the reduced relative humidity due to warmer temperature and/or reduced  
324 evaporation from the urban land cover, the so-called urban dry island effect (e.g., Hage, 1975;

Wang and Gong, 2009). The increase in cloud water in the afternoon is consistent with the enhanced updrafts. This mechanism potentially explains the increased frequency of extreme precipitation in urban areas in the afternoon (e.g. Craig and Bornstein, 2002; Rozoff et al., 2003; Wan et al., 2013; Zhong and Yang, 2015a, 2015b).

To understand the aerosol-induced reduction in extreme rainfall events, we analyze the diurnal cycle of aerosol effect (i.e., the difference LU70E06 and LU70E70) on radiative heating, vertical velocity, and net solar radiation at the surface (Fig. 11). As BC emission rates are relatively high in the YRD region (Fig. 2d), aerosols heat the atmosphere due to absorption of solar radiation during daytime (from 08:00 to 17:00 LST). As a result of absorption and scattering of solar radiation by aerosols, less solar radiation reaches the surface. These changes at the surface and in the atmosphere stabilize the atmosphere and reduce convective intensity in the afternoon (from 14:00 to 20:00 LST), which reduces the frequency of extreme rainfall events (Koren et al., 2004; Qian et al., 2006; Zhao et al., 2006; 2011; Fan et al., 2007). Although aerosols can enhance precipitation through cloud microphysical changes that invigorate convection (e.g., Khain et al., 2009; Rosenfeld et al., 2008; Fan et al., 2013), aerosol radiative effects generally dominate in China because of the high AOD and strong light-absorbing aerosol properties (Yang et al., 2011; Fan et al., 2015).

### **3.2.2 Synoptic influence on urbanization impacts**

The impacts of urbanization-induced UHI and aerosols on precipitation may be highly variable under different synoptic conditions that influence the atmospheric circulation and cloud and boundary layer processes. Precipitation changes due to urbanization effects may offset each other under different synoptic conditions, leading to an overall weak effect on mean precipitation



at longer time scales as discussed in section 3.2.1. We select two typical heavy late-afternoon  
 rainfall events with different background circulations over the YRD region. Case A occurred  
 from 08:00 LST 23 June to 08:00 LST 24 June 2006 and case B occurred from 08:00 LST 1 July  
 to 08:00 LST 2 July 2006. Figure 12a and 12d show the mean precipitation rate and 850 hPa  
 winds for case A and case B, respectively. Southwesterly flow dominates the entire region in case  
 A (Fig. 12a), while in case B (Fig. 12d) southwesterly and northwesterly winds dominate the  
 southern and northern parts of precipitation area, respectively. The averaged background wind  
 speed in case B is much stronger than that in case A, representing stronger synoptic forcing in  
 case B. The effects of urban land-cover change and aerosols on precipitation for the case A (case  
 B) are illustrated in Figs. 12b and 12c (Figs. 12e and 12f), respectively. Both cases show  
 significant precipitation responses to the forcing of urban land-cover and aerosols. We can see  
 that urban land cover increases the rainfall intensity in case A but aerosols decrease precipitation  
 over the urbanized area (Figs. 12b and 12c). The precipitation response to urban land cover and  
 aerosols is just the opposite in case B (Figs. 12e and 12f). Figs. 13a and 13d illustrate the  
 evolution of precipitation in region R1 (Fig. 12a) and R2 (Fig. 12d), respectively, for the two  
 cases. In both cases, rainfall mainly occurred between 08:00 LST and 20:00 LST. The  
 corresponding impacts of urban land-cover and aerosols are shown in Figs. 13b-c and Figs. 13e-f  
 for cases A and B, respectively. In case A, the urban land-cover substantially increases the  
 precipitation intensity in the afternoon with a maximum increase of  $6.87 \text{ mm h}^{-1}$ . Aerosol effects,  
 on the contrary, decrease the rainfall intensity with a maximum reduction of  $3.85 \text{ mm h}^{-1}$ . In case  
 B, however, effects of urban land-cover and enhanced aerosols on precipitation are opposite to  
 that in case A. A maximum rainfall reduction of  $3.81 \text{ mm h}^{-1}$  is found to be associated with the  
 effect of urban land cover and an increase of  $2.85 \text{ mm h}^{-1}$  is associated with the aerosol forcing.

370 Why do urban land-cover and aerosols exert opposite effects on precipitation during the  
 371 two rainfall events? Here we attempt to answer this question by examining the dynamical and  
 372 thermodynamical changes induced by the UHI and aerosols using the moisture flux convergence  
 373 (MFC), which is defined as:

$$374 \quad \text{MFC} = -\nabla \cdot (q\vec{V}_h) = -q\nabla \cdot \vec{V}_h - \vec{V}_h \cdot \nabla q \quad (2)$$

375 The first and second terms on the right hand side of Eq. 2 denote wind convergence (CON) and  
 376 moisture advection (MA), respectively.

377 Figures 14a and 14b illustrate the time-height cross sections of changes in moisture flux  
 378 convergence and cloud water mixing ratio induced by land-cover and aerosol changes over the  
 379 region R1 (Fig. 12a) during the rainy period in case A. Urban land-cover enhances the  
 380 convergence of moisture fluxes in the lower troposphere, which results in increased precipitation  
 381 (Fig. 14a). On the contrary, aerosols weaken the convergence of moisture fluxes and thus reduce  
 382 precipitation (Fig. 14b). These changes are consistent with those associated with extreme rainfall  
 383 changes shown in Fig. 10. Interestingly for case B over R2, urban land-cover weakens the  
 384 convergence of moisture fluxes (Fig. 14c) and thus suppresses precipitation (Fig. 13e) from  
 385 08:00 LST 1 July to 02:00 LST 2 July 2006. Aerosols, however, enhance the convergence of  
 386 moisture fluxes over R2 (Fig. 14d) and thus increase precipitation (Fig. 13f). These results  
 387 establish obvious correspondence between moisture flux convergence changes and the  
 388 precipitation response to urban land cover and aerosols in the two rainfall events and suggest  
 389 different processes may dominate the moisture flux convergence changes for the two cases.

390 Figure 15 presents the time-height cross section of the changes in the two terms of MFC,  
 391 i.e., CON (convergence) and MA (moisture advection), induced by land-cover and aerosol

changes averaged over R1 (Fig. 12a) for case A and over R2 (Fig. 12d) for case B. Urban land-cover enhances the wind convergence over R1 in case A (Fig. 15a), leading to an increase in CON by up to  $1.56 \times 10^{-4} \text{ g kg}^{-1} \text{ s}^{-1}$ , which is much larger than the increase of  $0.61 \times 10^{-4} \text{ g kg}^{-1} \text{ s}^{-1}$  averaged over R2 (Fig. 15c) in case B. The larger enhancement of convergence in case A is attributed to the strong UHI-induced surface heating during this rainfall period (figure not shown). In contrast, aerosols reduce the convergence in both case A and case B due to the aerosol cooling effect near the surface, as discussed previously (Fig. 11). The reduction of convergence in case A is more significant than that in case B because of the larger aerosol loading and, therefore, stronger surface cooling over R1 in case A (not shown). Urban land-cover reduces moisture advection in both cases, with a maximum decrease of  $-0.99$  and  $-1.89 \times 10^{-4} \text{ g kg}^{-1} \text{ s}^{-1}$ , respectively. Aerosols, however, increase moisture advection, and the maximum increases are  $0.93$  and  $1.31 \times 10^{-4} \text{ g kg}^{-1} \text{ s}^{-1}$  in case A and case B, respectively. Our results show clearly that the changes in CON are opposite to that in MA. As the impacts of urban land-cover and aerosols on moisture advection are greater in case B than in case A, the net changes in the moisture flux convergence are dominated by MA in case B and by CON in case A, leading to opposite effects between the two cases.

The significant differences in the responses of MA between the two cases are related to different background circulations during the two events (Figs. 12a and 12d). Weaker southwesterly flow dominates the entire region in case A (Fig. 12a), while in case B (Fig. 12d) stronger southwesterly and northwesterly winds dominate the southern and northern parts of precipitation area, respectively. The changes in MA could be further decomposed into three terms, as shown below in Eq. 3:

$$-\Delta \mathbf{V} \cdot \nabla \mathbf{q} = -\mathbf{V}_{\text{ctrl}} \cdot \Delta(\nabla \mathbf{q}) - (\nabla \mathbf{q})_{\text{ctrl}} \cdot \Delta \mathbf{V} - \Delta(\nabla \mathbf{q}) \cdot \Delta \mathbf{V} \quad (3)$$

Formatted: Font color: Red

The first term on the right-hand side of is associated with the change in water vapor, while the second term is associated with the change in circulation. The third term is a nonlinear term including the contribution of both the moisture and circulation changes. Figure 16 illustrates the changes in the first and second term, respectively. The contribution of the third nonlinear term is small and negligible compared to the other two terms (not shown). Urban land-cover reduces the first term in both cases, with a maximum decrease of  $-0.34$  and  $-1.54 \cdot 10^{-4} \text{ g kg}^{-1} \text{ s}^{-1}$ , respectively. Aerosols, however, increase the first term, and the maximum increases are  $0.49$  and  $1.78 \cdot 10^{-4} \text{ g kg}^{-1} \text{ s}^{-1}$  in case A and case B, respectively. The urban land-cover and aerosol effects on the second term are quite similar for both cases. Therefore, the most significant difference between these two cases is the change in the first term, which is directly associated with the background circulation. These changes in the first term are much larger in case B because of the stronger background winds than in case A, contributing to a more significant modification in MA as shown in Figure 15.

In summary, case B represents stronger synoptic forcing than case A. The stronger winds and larger spatial coverage of clouds and precipitation associated with the larger scale synoptic system weakens the UHI and aerosol effects through ventilation and changes in radiation, resulting in weaker CON and larger MA changes. Conversely, with weaker synoptic forcing, the stronger UHI and aerosol effects enhance the changes in CON while MA effects are smaller due to the weaker background winds. Therefore, our results highlight the distinguishing role of synoptic forcing on how urban land-cover and aerosol influence the dynamical and thermodynamical environments and precipitation.

#### 4. Summary

437 In this study, the state-of-the-art WRF-Chem model coupled with a single-layer UCM, is  
438 run at convection-permitting scale to investigate the influences of urbanization-induced land-  
439 cover change and elevated aerosol concentrations on local and regional climate in the Yangtze  
440 River Delta (YRD) in China. A 5-year period (2006-2010) is selected for multi-year simulations  
441 to investigate urbanization effects on extreme events and the role of synoptic forcing. Three  
442 experiments were conducted with different configurations of land cover and aerosol emissions:  
443 (1) urban land and emissions in 2006, (2) urban land in the 1970s and emissions in 2006, and (3)  
444 urban land and emissions in the 1970s. The experiment with the 2006 land-use type and  
445 anthropogenic emissions reproduces the observed spatial patterns of near-surface air temperature  
446 and precipitation fairly well.

447 The expanded urban land cover and increased aerosols have opposite impacts on the near-  
448 surface air temperature. The urban land-use change increases 2-m air temperature due to the UHI  
449 effect in commercial areas with a domain-averaged increase of 1.49 °C in summer and 0.7 °C in  
450 winter. In the surrounding areas, however, surface air temperature increases in summer but  
451 decreases in winter. The latter is attributed to the much greater thermal inertia over urban areas  
452 than over rural areas in wintertime when both vegetation cover and soil moisture are at their  
453 seasonal minimum. Compared to the effect of land-cover change, aerosol effect exerts a less  
454 significant influence on near-surface temperature with minor decreases in both summer and  
455 winter. Overall, the impact of urban land-use change outweighs that of enhanced aerosols on  
456 regional temperature especially in summer. The increase in near-surface temperature induced by  
457 the UHI effect leads to an increase in heat wave days by 3.7 days per year over the major mega  
458 cities in the YRD region. The greater response of solar radiation to urban land-cover in summer  
459 is the major factor contributing to the larger changes in surface temperature in summer than in

460 winter. Compared to the urban land-use effect, aerosol effect on reducing the surface solar  
461 radiation occurs over a much broader region including the downwind area of the city clusters.

462 The urban land-cover change and increased aerosols have opposite effects on the  
463 frequency of extreme rainfall during summer. The UHI effect leads to more frequent extreme  
464 precipitation over the urbanized area in the afternoon because of an enhanced near-surface  
465 convergence and vertical motion. In contrast, aerosol tends to decrease the frequency of extreme  
466 precipitation because of its cooling effect near the surface and heating effect (by light-absorbing  
467 particles) above, leading to an increased atmospheric stability and weakened updrafts. Additional  
468 aerosols can also induce decreases in the frequency of extreme precipitation over non-urban  
469 areas, particularly in the downwind area of the city clusters.

470 The effects of both urban land-cover and increased aerosols on summertime rainfall vary  
471 with synoptic weather systems and environmental conditions. Two late-afternoon rainfall events  
472 are selected for in-depth analysis. For the two cases, urbanization exerts similar impacts on local-  
473 scale convergence and mean wind speed, which modify the strength of moisture transport. More  
474 specifically, the effect of urban land-cover increases local-scale convergence due to the UHI-  
475 induced circulation and reduces low-level wind speed, while aerosols have an opposite effect due  
476 to the cooling near the surface. We found that the impacts of urban land-cover and aerosol on  
477 precipitation are determined not only by their effect on local-scale convergence, but also  
478 modulated by the large-scale weather systems. Our analyses suggest that synoptic forcing plays a  
479 significant role in how urbanization-induced land-cover and aerosols influence individual rainfall  
480 event. Although the two rainfall events selected for the analysis do not represent all types of  
481 precipitation events in the YRD Region, they demonstrate how the effect of urbanization on  
482 precipitation may vary and offset each other under different synoptic conditions, leading to an

483 overall weak effect on mean precipitation at longer time scales. To further quantify urbanization  
484 effects, uncertainties in anthropogenic emissions and heating, unresolved urban building and  
485 streets structure, and representation in aerosol-cloud interactions and cloud microphysics in the  
486 model should be investigated in future studies. Further investigation is also needed to have a  
487 better and more comprehensive understanding of the complicated mechanisms through which  
488 urbanization influences heavy rainfall under a full range of weather conditions.

## 489 **Acknowledgments** 490

491 The contributions of PNNL authors are supported by the U.S. Department of Energy's  
492 Office of Science as part of the Regional and Global Climate Modeling Program and  
493 Atmospheric System Research (ASR) program. The contribution of Shi Zhong and Xiu-Qun  
494 Yang is supported by the National Basic Research Program of China (2010CB428504), Jiangsu  
495 Collaborative Innovation Center for Climate Change, and the Scholarship Award for Excellent  
496 Doctoral Student granted by China Scholarship Council. The work of Ben Yang is supported by  
497 the National Natural Science Foundation of China (41305084). Computations were performed  
498 using resources of the National Energy Research Scientific Computing Center (NERSC) at  
499 Lawrence Berkeley National Laboratory and PNNL Institutional Computing. The Pacific  
500 Northwest National Laboratory is operated for DOE by Battelle Memorial Institute under  
501 contract DE-AC05-76RL01830. All model results are archived on a PNNL cluster and available  
502 upon request. Please contact Yun Qian (yun.qian@pnnl.gov).

503

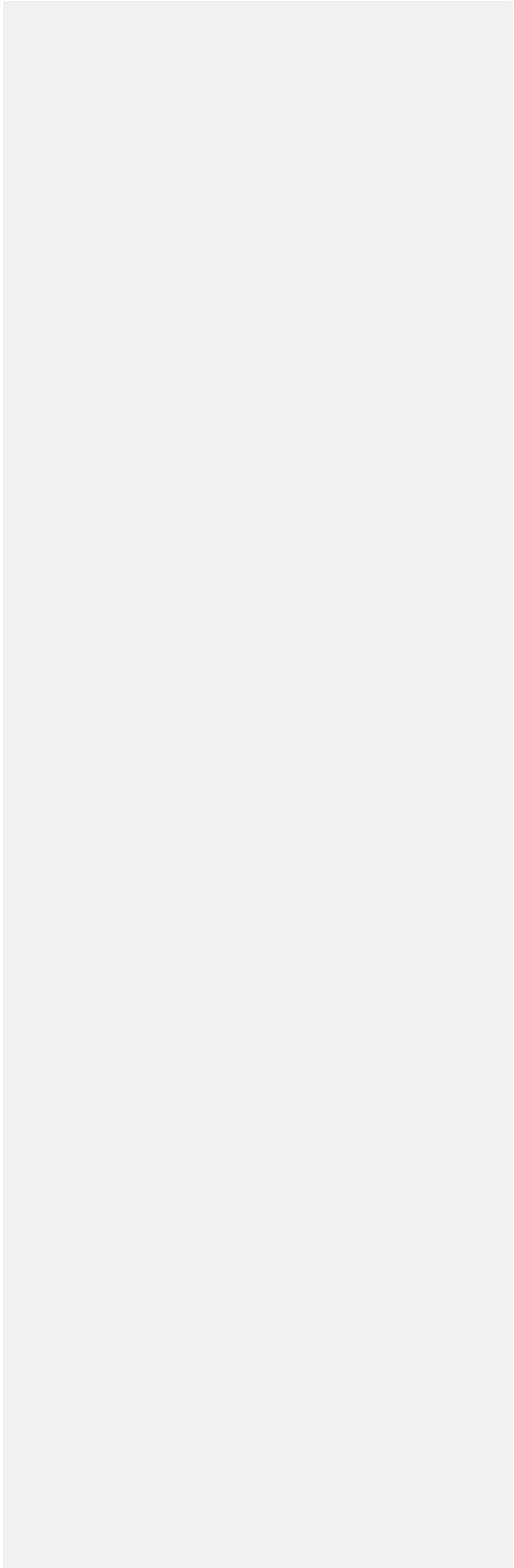
504

505

506

507

508





509 **Reference**

- 510 Baik, J. J., Kim, Y. H., Kim, J. J., and Han, J. Y.: Effect of boundary-layer stability on urban  
511 heat island induced circulation, *Theor. Appl. Climatol.*, 89, 73–81, 2007.
- 512 Bauer, S. E., and Menon, S.: Aerosol direct, indirect, semidirect, and surface albedo effects from  
513 sector contributions based on the IPCC AR5 emissions for preindustrial and present-day  
514 conditions, *J. Geophys. Res.*, 117, D01206, doi: 10.1029/2011JD016816, 2012.
- 515 Bornstein, R., and Lin, Q.: Urban heat islands and summertime convective thunderstorms in  
516 Atlanta: Three cases studies, *Atmos. Environ.*, 34, 507–516, 2000.
- 517 Braham, R. R.: Comments on “Urban, topographic and diurnal effects on rainfall in the St. Louis  
518 region”. *J. Appl. Meteorol.*, 18, 371-374, 1979.
- 519 Changnon, S. R.: Rainfall changes in summer caused by St. Louis, *Science*, 205, 402–404, 1979.
- 520 Charlson, R. J., et al.: Climate forcing by anthropogenic aerosols, *Science*, 255, 423–430, 1992.
- 521 Che, H. Z., Shi, G. Y., Zhang, X. Y., Arimoto, R., Zhao, J. Q., Xu, L., Wang, B., and Chen, Z. H.:  
522 Analysis of 40 years of solar radiation data from China, 1961–2000, *Geophys. Res. Lett.*,  
523 32, L06803, doi:10.1029/2004GL022322, 2005.
- 524 Chen, F., Kusaka, H., Bornstein, R., et al.: The integrated WRF/urban modeling system:  
525 development, evaluation, and applications to urban environmental problems, *Int. J.*  
526 *Climatol.*, 31(2), 273-288, 2001.
- 527 Coakley, J. A., Bernstein, R. L., and Durkee, P. A.: Effect of ship-track effluents on cloud  
528 reflectivity, *Science*, 273, 1020–1022, 1987.

529 Craig, K., and Bornstein, R.: MM5 simulation of urban induced convective precipitation over  
 530 Atlanta. Preprints, Fourth Conf. on the Urban Environment, Norfolk, VA, Amer. Meteor.  
 531 Soc., 5–6, 2002.

532 Dentener, F., et al.: Emissions of primary aerosol and precursor gases in the years 2000 and 1750  
 533 prescribed data-sets for AeroCom, Atmos. Chem. Phys., 6, 4321–4344, doi:10.5194/acp-6-  
 534 4321-2006, 2006.

535 Du, Y., et al.: Impact of urban expansion on regional temperature change in the Yangtze River  
 536 Delta, J. of Geophys. Sci., 17(4): 387-398, 2006.

537 Fast, J. D, et al.: Evolution of ozone, particulates, and aerosol direct forcing in an urban area  
 538 using a new fully-coupled meteorology, chemistry, and aerosol model, J. Geophys. Res.,  
 539 111, D21305, doi:10.1029/2005JD006721, 2006.

540 Fan, J., Leung, L. R., Rosenfeld, D., Chen, Q., Li, Z., Zhang, J., and Yan, H.: Microphysical  
 541 Effects Determine Macrophysical Response for Aerosol Impacts on Deep Convective  
 542 Clouds, Proceedings of the National Academy of Sciences of the United States of America,  
 543 110(48), E4581-E4590, doi:10.1073/pnas.1316830110, 2013.

544 Fan, J., Rosenfeld, D., Yang, Y., Zhao, C., Leung, Y. R., and Li, Z.: Substantial Contribution of  
 545 Anthropogenic Air Pollution to Catastrophic Floods in Southwest China, Geophys. Res.  
 546 Lett., 42(14), 6066-6075, doi:10.1002/2015GL064479, 2015.

547 Fan, J., Zhang, R., Li, G., Tao, W., and Li, X.: Simulations of cumulus clouds using a spectral  
 548 microphysics cloud resolving model, J. Geophys. Res., 112, D04201,  
 549 doi:10.1175/2010JAS3651.1, 2007.

550 Feingold G., Koren, I., Wang, H., Xue, H., and Brewer W.: Precipitation-generated oscillations in  
551 open cellular cloud fields. *Nature*, 466, 849–852, 2010.

552 Grell, G. A., Peckham, S. E., Schmitz, R., et al.: Fully coupled “online” chemistry within the  
553 WRF model, *Atmos. Environ.*, 39, 6957–6975, 2005.

554 Gustafson, W. I., Chapman, E. G., Ghan, S. J., Easter, R. C., and Fast, J. D.: Impact on modeled  
555 cloud characteristics due to simplified treatment of uniform cloud condensation nuclei  
556 during NEAQS 2004, *Geophys. Res. Lett.*, 34, L19809 doi:10.1029/2007GL0300321, 2007.

557 Guo, X., Fu, D., and Wang, J.: Mesoscale convective precipitation system modified by  
558 urbanization in Beijing city, *Atmos. Res.*, 82, 112–126, 2006.

559 Hage, K. D.: Urban-rural humidity difference, *J. Appl. Meteor.*, 14(7), 1277-1283, 1975.

560 Hansen, J., Sato, M., and Ruedy, R.: Radiative Forcing and Climate Response, *J. Geophys. Res.*,  
561 102, 6831–6864, 1997.

562 Hjermfelt, M. R.: Numerical simulation of the effects of St. Louis on mesoscale boundary layer  
563 airflow and vertical motion: Simulations of urban vs. non-urban effects, *J. Appl. Meteor.*,  
564 21, 1239–1257, 1982.

565 Hu, Y., Ban, Y., Zhang, Q., and Liu, J.: The trajectory of urbanization process in the Yangtze  
566 River Delta during 1990 to 2005. 7th Urban Remote Sensing Joint Event, 20–22 May 2009,  
567 Shanghai, DOI: 10.1109/URS.2009.5137536, 2009.

568 Huff, F. A., and Changnon Jr., S. A.: Climatological assessment of urban effects on precipitation  
569 at St. Louis, *J. Appl. Meteorol.*, 11, 823-842, 1972.

570 Inoue, T., and Kimura, F.: Urban effects on low-level clouds around the Tokyo metropolitan area  
 571 on clear summer days, *Geophys. Res. Lett.*, 31, L05103, doi:10.1029/2003GL018908, 2004.  
 572 Jauregui, E., Godinez, L., and Cruz, F.: Aspects of Heat-Island Development in Guadalajara,  
 573 Mexico, *Atmos. Environ.* 26B, 391–396, 1992.  
 574 Jiang Y, Liu, X., Yang, X. Q.: A numerical study of the effect of different aerosol types on East  
 575 Asian summer clouds and precipitation, *Atmos. Environ.*, 70, 51-63, 2013.  
 576 Kaufmann, R. K., Seto, K. C., Schneider, A., Liu, Z., Zhou, L., Wang, W.: Climate response to  
 577 rapid urban growth: evidence of a human-induced precipitation deficit, *J. Climate*, 20(10),  
 578 2299-2306, 2007.  
 579 Khain A. P.: Notes on state-of-the-art investigations of aerosol effects on precipitation: a critical  
 580 review, *Environ. Res. Lett.*, 4(1), 015004, 2009.  
 581 Koren, I., et al.: Measurement of the effect of Amazon smoke on inhibition of cloud formation,  
 582 *Science*, 303(5662), 1342-1345, 2004.  
 583 Kusaka, H., Kikegawa, Y., and Kimura, F.: A simple single layer urban canopy model for  
 584 atmospheric models: comparison with multi-layer and slab models, *Bound-Layer Meteor.*,  
 585 101, 329–358, 2001.  
 586 Landsberg, H. E.: *The Urban Climate*, Academic Press, London, UK, 1981.  
 587 Lei, M., et al.: Effect of explicit urban land surface representation on the simulation of the 26  
 588 July 2005 heavy rain event over Mumbai, India, *Atmos. Chem. Phys.*, 8 (20), 5975-5995,  
 589 2008.

590 Lu, Z., Zhang, Q., and Streets, D. G.: Sulfur dioxide and primary carbonaceous aerosol  
 591 emissions in China and India, 1996–2010, *Atmos. Chem. Phys.*, 11(18), 9839–9864, 2011.  
 592 Masterson, J., Richardson F. A.: Humidex. A method of quantifying human discomfort due to  
 593 excessive heat and humidity, Environment Canada, Downsview, 1979.  
 594 McFarquhar, G. M., and H. Wang: Effects of aerosols on trade wind cumuli over the Indian  
 595 Ocean: Model simulations, *Q. J. R. Meteorol. Soc.*, 132, 821–843, 2006.  
 596 Miao, S. G., Chen, F., Li, Q. C., and Fan, S. Y.: Impacts of urban processes and urbanization on  
 597 summer precipitation: a case study of heavy rainfall in Beijing on 1 August 2006, *J. Appl.*  
 598 *Meteorol. Climatol.*, 50, 806–825, 2010.  
 599 Monin, A. S., and Obukhov, A. M.: Basic laws of turbulent mixing in the surface layer of the  
 600 atmosphere, *Contributions of the Geophysical Institute of the Slovak Academy of*  
 601 *Sciences*, 24, 151, 163–187, 1954.  
 602 Oke, T. R.: The Energetic Basis of the Urban Heat Island, *Q. J. R. Met. Soc.*, 108, 1–22, 1982.  
 603 Oke, T. R.: *Boundary Layer Climates*. 2d ed. Methuen Co., 435 pp, 1987.  
 604 Oleson, K. W., Bonan, G. B., Feddema, J., and Vertensten, M.: An urban parameterization for a  
 605 global climate model. Part II: Sensitivity to input parameters and the simulated urban heat  
 606 island in offline simulations, *J. Appl. Meteor. Climatol.*, 47, 1061–1076, 2008.  
 607 Qian, Y., Kaiser, D. P., Leung, L. R., and Xu, M.: More frequent cloud-free sky and less surface  
 608 solar radiation in China from 1955 to 2000, *Geophys. Res. Lett.*, 33, L01812,  
 609 doi:10.1029/2005GL024586, 2006.

610 Qian, Y., Wang, W., Leung, L. R., and Kaiser, D. P.: Variability of solar radiation under cloud-  
611 free skies in China: The role of aerosols, *Geophys. Res. Lett.*, 34, L12804,  
612 doi:10.1029/2006GL028800, 2007.

613 Qian, Y., Gong, D., Fan, J., Leung, L. R., Bennartz, R., Chen, D., Wang, W.: Heavy pollution  
614 suppresses light rain in China: Observations and modeling, *J. Geophys. Res.*, 114, D00K02,  
615 doi:10.1029/2008JD011575, 2009.

616 Qian, Y., Gustafson Jr, W. I., and Fast, J. D.: An investigation of the sub-grid variability of trace  
617 gases and aerosols for global climate modeling, *Atmos. Chem. Phys.*, 10, 6917-6946,  
618 doi:10.5194/acp-10-6917-2010, 2010.

619 Qian, Y., Teppe, J., Yasunari, J., et al.: Light-absorbing particles in snow and ice: Measurement  
620 and modeling of climatic and hydrological impact. *Adv. Atmos. Sci.*, 32(1), 64–91, doi:  
621 10.1007/s00376-014-0010-0, 2015.

622 Ren, G., Zhou, Y., Chu, Z., Zhou, J., Zhang, A., Guo, J., Liu, X.: Urbanization Effects on  
623 Observed Surface Air Temperature Trends in North China, *J. Climate*, 21 (6), 1333-1348,  
624 2008.

625 Rosenfeld, D.: Suppression of rain and snow by urban and industrial air pollution, *Science*, 287  
626 (5459), 1793-1796, 2000.

627 Rosenfeld, D., et al.: Flood or drought: How do aerosols affect precipitation? *Science*, 321,  
628 1309–1313, doi:10.1126/science.1160606, 2008.

629 Rozoff, C., Cotton, W. R., and Adegoke, J. O.: Simulation of St. Louis, Missouri, land use  
630 impacts on thunderstorms, *J. Appl. Meteor.*, 42, 716–738, 2003.

631 Schell, B., Ackermann, I. J., Hass, H., Binkowski, F. S., and Ebel, A.: Modeling the formation of  
 632 secondary organic aerosol within a comprehensive air quality modeling system, *J. Geophys.*  
 633 *Res.*, 106, 28275–28293, 2001.

634 Sen Roy, S., and Yuan, F.: Trends in extreme temperatures in relation to urbanization in the Twin  
 635 Cities Metropolitan Area, Minnesota. *J. Appl. Meteor.*, 48 (3), 669-679, 2009.

636 Shepherd, J. M., and Burian, S. J.: Detection of urban-induced rainfall anomalies in a major  
 637 coastal city, *Earth Interactions*, 7(4), 1-17, 2003.

638 Shepherd, J. M., Carter, M., Manyin, M., Messen, D., and Burian, S.: The impact of urbanization  
 639 on current and future coastal precipitation: a case study for Houston, *Environ. Plan.*, 37,  
 640 284-304, 2010.

641 Shepherd, J. M.: A review of current investigations of urban-induced rainfall and  
 642 recommendations for the future, *Earth Interact.*, 9 (12), 1-27, 2005.

643 Skamarock, W. C., Klemp, J. B.: A time-split nonhydrostatic atmospheric model for weather  
 644 research and forecasting applications, *J. Computational Physics*, 227(7): 3465-3485,  
 645 2008.

646 Stone, B.: *The city and the coming climate: Climate change in the places we live*, Cambridge  
 647 University Press, New York, 2012.

648 Stockwell, W. R., Middleton, P., Chang, J. S., and Tang, X.: The second generation regional acid  
 649 deposition model chemical mechanism for regional air quality modeling, *J. Geophys. Res.*,  
 650 95, 16343–16367, 1990.

651 Storer R. L., and Van den Heever, S. C.: Microphysical processes evident in aerosol forcing of  
652 tropical deep convective clouds, *J. Atmos. Sci.*, 70(2), 430-446, 2013.

653 Tan J., Kalkstein, L. S., Huang, J., Lin, S., Yin, H., Shao, D.: An operational heat/health warning  
654 system in Shanghai, *International Journal of Biometeorology*, 48(3), 157-162, 2004.

655 Tao, W. K., Chen, J. P., Li, Z., Wang, C., Zhang, C.: Impact of aerosols on convective clouds and  
656 precipitation, *Rev. Geophys.*, 50 (2), 2012.

657 Tewari, M., Chen, F., Kusaka, H., and Miao, S.: Coupled WRF/Unified Noah/urban-canopy  
658 modeling system, NCAR WRF Documentation. Boulder: NCAR, 1-20, 2007.

659 Wan, H. C., Zhong, Z., Yang, X. Q., and Li, X. Q.: Impact of city belt in Yangtze River Delta in  
660 China on a precipitation process in summer: A case study, *Atmos. Res.*, 125-126, 63–75,  
661 2013.

662 Wang, H., and Feingold, G.: Modeling mesoscale cellular structures and drizzle in marine  
663 stratocumulus. Part II: The Microphysics and Dynamics of the Boundary Region between  
664 Open and Closed Cells, *J. Atmos. Sci.*, 66, 3257–3275, 2009.

665 Wang, H., Skamarock, W. C., and Feingold, G.: Evaluation of scalar advection schemes in the  
666 Advanced Research WRF model using large-eddy simulations of aerosol–cloud  
667 interactions, *Mon. Wea. Rev.*, **137**, 2547–2558, 2009.

668 Wang, X. Q., and Gong, Y. B.: The impact of an urban dry island on the summer heat wave and  
669 sultry weather in Beijing City, *Chinese Science Bulletin*, 55(16), 1657-1661, 2010.



670 Wang, Y., Zhuang, G., Zhang, X., Huang, K., Xu, C., Tang, A., Chen, J., An, Z.: The ion  
 671 chemistry, seasonal cycle, and sources of PM<sub>2.5</sub> and TSP aerosol in Shanghai, *Atmos.*  
 672 *Environ.*, 40(16), 2935-2952, 2006.

673 Wang, K. C., Wang, J., Wang, P., Sparrow, M., Yang, J., Chen, H.: Influences of urbanization on  
 674 surface characteristics as derived from the Moderate-Resolution Imaging  
 675 Spectroradiometer: A case study for the Beijing metropolitan area, *J. Geophys. Res.*, 112.  
 676 D22S06, 2007.

677 Wang, X. M., Sun, X. G., Tang, J. P., and Yang, X. Q.: Urbanization-induced regional warming in  
 678 Yangtze River Delta: potential role of anthropogenic heat release, *Int. J. Climatol.*, doi:  
 679 10.1002/joc.4296, 2015.

680 Wienert, U., and Kuttler, W.: The dependence of the urban heat island intensity on latitude—a  
 681 statistical approach, *Meteorologische Zeitschrift*, 14(5), 677-686, 2005.

682 Wu, Kai, and Yang, X. Q.: Urbanization and heterogeneous surface warming in eastern China,  
 683 *Chinese Science Bulletin*, 58 (12), 1363-1373, 2013.

684 Yang, Ben, Zhang, Y. C., and Qian, Y.: Simulation of urban climate with high-resolution WRF  
 685 model: A case study in Nanjing, China, *Asia-Pacific J. Atmos. Sci.*, 48 (3), 227-241, 2012.

686 Yang, X., Hou, Y., Chen, B.: Observed surface warming induced by urbanization in east China, *J.*  
 687 *Geophys. Res.*, 116 (D14), 2011.

688 Yu, H., Kaufman, Y. J., Chin, M., et al.: A review of measurement-based assessments of the  
 689 aerosol direct radiative effect and forcing, *Atmos. Chem. Phys.*, 6 (3), 613-666, 2006.

690 Zhang, N., Gao, Z., Wang, X., Chen, Y.: Modeling the impact of urbanization on the local and  
691 regional climate in Yangtze River Delta, China, *Theor. Appl. Climatol.*, 102(3-4): 331-342,  
692 2010.

693 Zhang, Q., Hu, Y., Liu, J.: The trajectories of urban land and industrial land in Shanghai over the  
694 past 30 years, *Urban Remote Sensing Event, 2009 Joint. IEEE*, 2009a.

695 Zhang, Q., Streets, D. G., Carmichael, G. R., et al.: Asian emissions in 2006 for the NASA  
696 INTEX-B mission, *Atmos. Chem. Phys.*, 9, 5131–5153, doi:10.5194/acp-9-5131-2009,  
697 2009b.

698 Zhao, C., Tie, X., Lin, Y.: A possible positive feedback of reduction of precipitation and increase  
699 in aerosols over eastern central China, *Geophys. Res. Lett.*, 33(11), 2006.

700 Zhao, C., Liu, X., Leung, L. R., Johnson, B., MaFarlane, S. A., Gustafson, W. I., Fast, J. D.,  
701 Easter, R.: The spatial distribution of mineral dust and its shortwave radiative forcing  
702 over North Africa: modeling sensitivities to dust emissions and aerosol size treatments,  
703 *Atmos. Chem. Phys.*, 11, 1879-1893, 2010.

704 Zhao, C., Liu, X., Leung, L. R., and Hagos, S.: Radiative impact of mineral dust on monsoon  
705 precipitation variability over West Africa, *Atmos. Chem. Phys.*, 11, 1879-1893,  
706 doi:10.5194/acp-11-1879-2011, 2011.

707 Zhao, C., Leung, L. R., Easter, R., Hand, J., and Avise, J.: Characterization of speciated aerosol  
708 direct radiative forcing over California, *J. Geophys. Res.*, 118, 2372–2388,  
709 doi:10.1029/2012JD018364, 2013a.

710 Zhao, C., Chen, S., Leung, L. R., Qian, Y., Kok, J., Zaveri, R., and Huang, J.: Uncertainty in  
711 modeling dust mass balance and radiative forcing from size parameterization, *Atmos.*  
712 *Chem. Phys.*, 13, 10733–10753, 2013b.

713 Zhong, S., and Yang, X. Q.: Ensemble simulations of the urban effect on a summer rainfall event  
714 in the Great Beijing Metropolitan Area, *Atmos. Res.*, 153, 318-334. 2015a.

715 Zhong, S., and Yang, X. Q.: Mechanism of urbanization impact on a summer cold frontal rainfall  
716 process in the Great Beijing Metropolitan Area, *J. Appl. Meteorol. Climatol.*, doi:  
717 10.1175/JAMC-D-14-0264.1, 2015b.

718 Zhong, S., Qian, Y., Zhao, C., Leung, R., and Yang, X. Q.: A case study of urbanization impact  
719 on summer precipitation in the Greater Beijing Metropolitan Area: Urban heat island  
720 versus aerosol effects, *J. Geophys. Res. Atmos.*, 120, doi:10.1002/2015JD023753, 2015.

721

722

723

724

725

726

727

728 **Table and Figure Captions**

729 **Table 1** Configurations of the WRF physics schemes used in the present study.

730 **Table 2** Numerical experiments and corresponding urban land use and aerosol emissions.

731 **Table 3** Analysis strategies for the investigation of urban land-use and/or aerosol effects.

732 **Figure 1** Land-use categories for year (a) 1970; (b) 2006; and (c) SO<sub>2</sub> (units: mol km<sup>-2</sup> h<sup>-1</sup>) and  
733 (d) black carbon (BC) emission rates (units: ug m<sup>-2</sup> s<sup>-1</sup>) averaged over 2006-2010. Surface  
734 topography is also shown in Fig. 1a (contour; units: m). The boxes in Fig. 1b outline three mega-  
735 city clusters of Nanjing, Su-Xi-Chang, and Shanghai.

736 **Figure 2** Moving spatial anomalies of averaged surface skin temperature (units: °C) with a  
737 filtering window size of 1° × 1° for (a) MODIS observation and (b) the L06E06 simulation. The  
738 “High Intensity Residential” and “Commercial/Industrial/Transportation” areas are marked with  
739 green lines and yellow lines, respectively.

740 **Figure 3** Annual mean (a) near-surface temperature (units: °C) and (b) precipitation (units: mm  
741 d<sup>-1</sup>) from observations (shaded circles) and the LU06E06 simulation (shaded).

742 **Figure 4** Differences in mean 2-m temperature (Units: °C) between simulations (a, d) LU06E70  
743 and LU70E70, (b, e) LU70E06 and LU70E70, (c, f) LU06E06 and LU70E70 for summer (upper  
744 panels) and winter (bottom panels). “Commercial/Industrial/Transportation” areas are marked  
745 with green lines. The black dots mark the area with statistically significant changes.

746 **Figure 5** Differences in net shortwave fluxes at the surface (units:  $\text{W m}^{-2}$ ) between simulations  
747 (a, c) LU06E70 and LU70E70, and (b, d) LU70E06 and LU70E70 in summer (upper panels) and  
748 winter (bottom panels).

749 **Figure 6** Differences in column burden of PM<sub>2.5</sub> ( $\text{g m}^{-2}$ ) between simulations LU70E06 and  
750 LU70E70, superimposed with near-surface winds simulated in LU70E70, for (a) summer and (b)  
751 winter.

752 **Figure 7** Differences in mean summertime (a) heat wave days (units: d/yr) and (b) heat stress  
753 (units:  $^{\circ}\text{C}$ ) between simulations LU06E70 and LU70E70.

754 **Figure 8** Diurnal cycles of the frequency of summertime extreme rainfall events for LU70E70  
755 (defined using hourly precipitation intensity above 95<sup>th</sup> percentile, black lines, right axis) and the  
756 differences between simulations over (a) Nanjing, (b) Shanghai, and (c) Su-Xi-Chang. Red lines  
757 are for Land use effect, blue lines for Aerosol effect, and green lines for the combined effect.

758 **Figure 9** Differences in the frequency of summertime extreme rainfall events (averaged from  
759 12:00 to 20:00 LST) between simulations (a) LU06E70 and LU70E70, and (b) LU70E06 and  
760 LU70E70.

761 **Figure 10** (a) Time-height cross-sections of differences (between LU06E70 and LU70E70) in  
762 temperature (contour; units:  $^{\circ}\text{C}$ ) and divergence (shade; units:  $10^{-5} \text{ s}^{-1}$ ) averaged over the three  
763 city clusters (Nanjing, Shanghai, and Su-Xi-Chang); (b) same as (a), but for vertical velocity  
764 (shade; units:  $10^{-2} \text{ m s}^{-1}$ ) and cloud water mixing ratio (contour;  $10^{-3} \text{ kg kg}^{-1}$ ).

765 **Figure 11** Time-height cross-sections of differences between LU70E06 and LU70E70 in  
766 radiative heating profile (shade; units:  $\text{K d}^{-1}$ ), vertical velocity (contour; units:  $10^{-2} \text{ m s}^{-1}$ ) and

767 surface solar radiation (blue bars; units:  $\text{W m}^{-2}$ ) averaged over the three city clusters (Nanjing,  
768 Shanghai, and Su-Xi-Chang).

769 **Figure 12** Rain rate (units:  $\text{mm h}^{-1}$ ) superimposed with wind vectors at 850 hPa for case A from  
770 08:00 LST 23 June to 08:00 LST 24 June 2006 (a) simulated in the LU06E06 simulation, (b)  
771 differences between LU06E70 and LU70E70, (c) differences between LU70E06 and LU70E70.  
772 Panels (d-f) are the same as (a-c) but for case B from 08:00 LST 1 July to 08:00 LST 2 July  
773 2006. The boxes R1 in (a) and R2 in (d) outline the three regions over which further analysis are  
774 conducted. Lines across the center of each box mark the cross-sections to be analyzed.

775 **Figure 13** The time evolution of precipitation (units:  $\text{mm h}^{-1}$ ) along the line *ab* (marked in Fig.  
776 12a) from 08:00 LST 23 June to 02:00 LST 24 June 2006 (case A) (a) simulated in the LU06E06  
777 simulation, (b) differences between LU06E70 and LU70E70, (c) differences between LU70E06  
778 and LU70E70. Panels (d-f) are the same as (a-c) but for case B along line *cd* (marked in Fig.  
779 12d) from 08:00 LST 1 July to 02:00 LST 2 July 2006.

780 **Figure 14** The time-height cross-sections of differences in moisture flux convergence (shaded;  
781 units:  $10^{-4} \text{ g}^{-1} \text{ kg}^{-1} \text{ s}^{-1}$ ) and water vapor mixing ratio (black lines; units:  $10^{-2} \text{ g kg}^{-1}$ ) from 08:00  
782 LST 23 June to 02:00 LST 24 June 2006 (case A) over region R1 (denoted in Fig. 12a) between  
783 (a) LU06E70 and LU70E70; (b) LU70E06 and LU70E70; Panels (c, d) are the same as (a, b) but  
784 for case B from 08:00 LST 1 July to 02:00 LST 2 July 2006 over R2 (denoted Fig. 12d).

785 **Figure 15** Same as Fig. 14 but for differences in the CON term (shaded; units:  $10^{-4} \text{ g}^{-1} \text{ kg}^{-1} \text{ s}^{-1}$ )  
786 and MA term (black lines; units:  $10^{-4} \text{ g}^{-1} \text{ kg}^{-1} \text{ s}^{-1}$ ) in eq. (2).

787 **Figure 16** Same as Fig. 15 but for differences in-the first term  $(-V_{\text{ctrl}} \cdot \Delta(\nabla q))$  (shaded; units:  $10^{-4}$   
788  $\text{g}^{-1} \text{kg}^{-1} \text{s}^{-1}$ ) and the second term  $(-(\nabla q)_{\text{ctrl}} \cdot \Delta V)$  (black lines; units:  $10^{-4} \text{g}^{-1} \text{kg}^{-1} \text{s}^{-1}$ ) in Eq.3.